Title Page

Title:

Recognition of the Nucleotide-Dependent Feature Facilitates the Microtubule End-Binding of MCAK

Authors and affiliations:

Wei Chen[1] (chenwill@mail.tsinghua.edu.cn)
Yin-Long Song[1] (y.song4@uu.nl)
Jian-Feng He[1] (jianfenghe2015@mail.tsinghua.edu.cn)
Xin Liang[1,*] (xinliang@tsinghua.edu.cn)

[1] IDG/McGovern Institute for Brain Research, School of Life Sciences, Tsinghua University, Beijing 100084, China

Corresponding author:

Name: Xin Liang
Address: Room E118, Medical School, Tsinghua University, 100084 Beijing, China
Tel: +86-10-62772563
Email: xinliang@tsinghua.edu.cn
ORCID: 0000-0001-7915-8094

Key words

MCAK
Microtubule dynamics
End binding
Depolymerization
GTP cap

Recognition of the Nucleotide-Dependent Feature Facilitates the Microtubule End-Binding of MCAK

Wei Chen[1], Yin-Long Song[1], Jian-Feng He[1], Xin Liang[1,*]

[1] IDG/McGovern Institute for Brain Research, School of Life Sciences, Tsinghua University, Beijing 100084, China

* Correspondence: xinliang@tsinghua.edu.cn

Abstract

The growing plus-end is a key regulatory site for microtubule dynamics. MCAK (mitotic centromere-associated kinesin), a microtubule depolymerizing kinesin, is an end-binding regulator of catastrophe frequency. It is intriguing how MCAK specifically binds to dynamic microtubule ends. Here, we measure the end-binding kinetics of MCAK using single-molecule imaging and reveal the end-binding preference. MCAK binds to the entire GTP cap, including the EB cap and the distalmost cap. Further analysis shows that MCAK strongly binds to GTPγS microtubules, suggesting that it could recognize the nucleotide-dependent feature of microtubules. Moreover, the binding preference is independent on the nucleotide state of MCAK, and this feature facilitates the high-affinity end-binding of MCAK. Finally, we show that despite partially sharing the binding regions, MCAK and XMAP215 function in an additive manner, demonstrating a simple logic of how the end-binding regulators work in coordination. In all, our results provide novel insights into understanding how MCAK regulates the dynamics of microtubule ends.

(156 words)

Introduction

Microtubule is a major type of cytoskeleton in eukaryotic cells and supports many cellular processes, such as cell division, polarization and migration (Alberts, 2015). However, the properties of microtubules vary a lot in different cellular processes and structures (Janke and Magiera, 2020; Kapitein and Hoogenraad, 2015; Wittmann et al., 2001). The plasticity implies that cellular microtubules are under complex and accurate regulations. Because microtubule-associated proteins (MAPs) are important components in the regulatory networks of microtubules, their functions and working mechanisms are key to understand cellular regulations on microtubules.

Not only do kinesin superfamily members move cargoes along microtubules, they also act as regulators of microtubule dynamics, for example, the depolymerizing kinesins (e.g. the kinesin-8 and kinesin-13 family members). Kinesin-13 was initially identified in studying spindle functions and neurons (Aizawa et al., 1992; Noda et al., 1995; Walczak et al., 1996; Wordeman and Mitchison, 1995). Later, the functions of kinesin-13 were revealed in more cellular processes, including spindle assembly (Walczak et al., 2002), chromosome segregation (Kline-Smith et al., 2004), directional migration (Zong et al., 2021), ciliary length control (Piao et al., 2009; Vasudevan et al., 2015), and neuronal polarization (Ghosh-Roy et al., 2012; Puri et al., 2021). The loss of kinesin-13 often alters structural and dynamic properties of cellular microtubules, implying that the kinesin-13 class members play regulatory roles. In addition, the subcellular localizations of kinesin-13, such as growing microtubule ends, centrosome and centromere, are active regulatory sites of microtubule dynamics in cells, further suggesting the functions of the kinesin-13 class members in controlling the length, mass and polarity of microtubules in cells.

As a representative model for the kinesin-13 family, MCAK was shown to be a microtubule depolymerase and a catastrophe factor (Desai et al., 1999; Gardner et al., 2011; Hunter et al., 2003). Biochemical and structural analysis suggests that MCAK could deconstruct the protective end structure of dynamic microtubules, and it does so by bending and then breaking off the underlying substrate (i.e. terminal tubulin dimers or protofilaments) (Moores and Milligan, 2006). It was proposed that MCAK targets microtubule ends by rapid lattice diffusion or binding to the end-binding proteins (EBs) (Gouveia et al., 2010; Helenius et al., 2006; Honnappa et al., 2009). Furthermore, the direct binding of MCAK to growing microtubule ends was also observed (Gouveia et al., 2010), implying the presence of specific end-binding sites. Previous studies on the structures of MCAK, propose that MCAK targets to microtubule ends by recognizing the curved protofilaments (Asenjo et al., 2013; Benoit et al., 2018; Tan et al., 2008; Trofimova et al., 2018; Wang et al., 2017). This was mostly based on the findings on stabilized microtubules, short protofilaments or tubulin dimers. It still remains elusive how MCAK binds to dynamic microtubule ends.

In the present study, we characterize the direct binding of MCAK to growing microtubule ends using single-molecule imaging. The key finding is that MCAK binds

to the entire GTP cap, including both the EB cap, where GDP·Pi-tubulin dimers are thought to gather, and the distalmost cap, where XMAP215 binds to curved protofilament (mostly in GTP state). The high-affinity binding of MCAK to the EB cap was intriguing. Further analysis shows that MCAK strongly binds to GTPγS microtubules, thought to be the analogue of GDP·Pi-tubulins. Therefore, we think that MCAK could recognize the nucleotide-dependent feature at dynamic microtubule ends. Moreover, the mutant studies show that the binding-preference of MCAK for GDP·Pi-tubulins facilitates the end-binding and in turn the function of MCAK. Finally, we find that despite having partially overlapped binding regions, MCAK and XMAP215 could precisely specify their regulatory function at dynamic microtubule end, thereby providing novel insights in understanding how microtubule-associated proteins functionally orchestrate at growing microtubule ends.

Results

MCAK shows a binding preference for growing microtubule ends

We set off by measuring the single-molecule binding kinetics of MCAK at growing microtubule ends using the *in vitro* microtubule dynamics assay. This experiment was performed in BRB80 supplemented with 50 mM KCl and 1 mM ATP, providing a nearly physiological ion strength. In this condition, the individual binding events of MCAK can be observed at both the end and the lattice (**Fig. 1A**). By measuring the fluorescence intensity of these binding events, we confirmed that they reflected individual MCAK dimers (**Fig. s1**). Using an in-house software (Song et al., 2020), we determined the binding position of individual MCAK molecules at subpixel resolution by fitting a Gaussian function to their intensity profile along the long axis of microtubules (**Fig. 1B**). Using the position of the plus-end as the spatial reference, we overlaid the end-binding of 152 MCAK molecules (**Fig. 1C**). The distribution showed that the binding regions of MCAK had a length of 162 nm (FWHM, the Full Width at Half Maximum), about 20 layers of tubulin dimers. We defined the binding events of MCAK within this region as "end binding" and those on the lattice as "lattice binding" (**Fig. 1A**).

To understand the binding kinetics, we first compared the apparent association rates of MCAK on the plus-end ($k_{on\text{-}P}$) and lattice ($k_{on\text{-}L}$) in the presence of ATP. The ratio ($R_{E/L}$) of $k_{on\text{-}P}$ ((22. 6 ± 1.4) $\times 10^{-6}$ s^{-1} nM^{-1}, per tubulin dimer, hereinafter) and $k_{on\text{-}L}$ ((2.8 ± 0.3) $\times 10^{-6}$ s^{-1} nM^{-1}) was 13 ± 1 (n=66 microtubules from 3 assays) (**Fig. 1 D-E**). We then measured the dwell time, which reflects the dissociation rate (k_{off}) (**Fig. s1**). The mean dwell time of MCAK on the lattice was shorter than that at the plus-end (plus end: 0.75 ± 0.02 s, n=966 events from 3 assays; 0.62 ± 0.02 s, n=702 events from 3 assays, p<0.001) (**Fig. 1F**). Using these kinetic parameters, we calculated the dissociation constant (K_d) of MCAK for the plus-end ($K_{d\text{-}P}$ =69 μM) and lattice ($K_{d\text{-}L}$=1057 μM), respectively. Therefore, MCAK shows a clear end-binding preference. We also observed single-molecule binding events of MCAK to the minus-end (**Fig. 1A**). Given the higher physiological relevance, we focused on the plus-end binding events (referred to as "end-binding" hereinafter) in the following analysis.

To understand the influence of the nucleotide state, we measured the end-binding kinetics of MCAK·AMPPNP, MCAK·ADP or MCAK·APO (the nucleotide-free state). First, the $k_{on\text{-}P}$ and $k_{on\text{-}L}$ of MCAK·AMPPNP were both reduced in comparison to that of MCAK·ATP (**Fig. 1 D-E**), resulting in an end-binding preference ($R_{E/L}$=11 ± 2, n=29 microtubules from 2 assays, p>1) that is similar to that of MCAK·ATP. Meanwhile, the end-binding of MCAK·AMPPNP showed a longer dwell time (3.32 ± 0.24 s, n=231 events from 2 assays, p<0.001), indicating a lower k_{off} (**Fig. 1F and Fig. s1**). As a result of the proportionally reduced $k_{on\text{-}P}$ and k_{off}, the end-binding affinity ($K_{d\text{-}P}$=61 μM) of MCAK·AMPPNP was similar to that of MCAK·ATP. Second, MCAK·ADP showed a nearly unchanged $k_{on\text{-}P}$ and an increased $k_{on\text{-}L}$, leading to a smaller $R_{E/L}$ (2 ± 0.3, n=21 microtubules from 2 assays, p<0.001) and suggest a re-

duced, but not the absence of, end-binding preference (**Fig. 1 D-E**). Meanwhile, it showed a significantly shorter end-binding dwell time (0.46 ± 0.02 s, n=327 events from 2 assays, p<0.001) than MCAK·ATP (**Fig. 1 F**). Therefore, MCAK·ADP has a lower end-binding affinity ($K_{d\text{-}P}$=163 μM). Third, APO·MCAK showed an increase in $k_{on\text{-}P}$ and an even greater increase in $k_{on\text{-}L}$, thereby having a smaller $R_{E/L}$ (2 ± 0.2, n=36 microtubules from 3 assays, p<0.001) (**Fig. 1 D-E**). It also showed a significantly longer end-binding dwell time (1.89 ± 0.23 s, n=71 events from 3 assays, p<0.001) (**Fig. 1 F**), suggesting a lower k_{off} (**Fig. s1**). Therefore, in comparison to MCAK·ATP, MCAK·APO possesses a higher end-binding affinity ($K_{d\text{-}P}$=1.8 μM) but partially loses the end-binding preference. Based on these measurements, we conclude that the end-binding preference and affinity of MCAK depend on its nucleotide state (see **Discussion**).

Having measured the end-binding kinetics, we were able to calculate whether the binding of MCAK on dynamic microtubule ends is due to direct end-binding (3D diffusion) or 1D lattice-diffusion (Gouveia et al., 2010; Helenius et al., 2006). Note that these two mechanisms are not mutually exclusive. Using our dataset, we measured that the lattice-diffusion coefficient of MCAK (*D*) on the lattice of dynamic microtubules was 0.023 ± 0.001 $\mu m^2 \cdot s^{-1}$ (**Fig. 1G**), close to the previously reported value (Cooper et al., 2010). Because the dwell time of the lattice-binding events was ~0.6 s, the average length scanned by a MCAK molecule via 1D lattice-diffusion was ~160 nm. Note that this is close to the length the GTP cap. Using a previously reported Fick's first equation of diffusion (Helenius et al., 2006), we calculated the flux of MCAK reaching growing ends via 1D diffusion was 0.004 s^{-1}. This was significantly lower than the arrival rate of MCAK onto the plus end observed in our experiments ($N_p = k_{on} \cdot C$ =0.067 s^{-1}. *C*: MCAK concentration). Therefore, in our experimental condition, 1D lattice-diffusion makes a minor contribution to the end-binding of MCAK (~ 6%), and the end-binding of MCAK can be thought of as the direct interaction between diffusive MCAK and the end structure.

MCAK binds to the entire GTP cap

Having recorded and analyzed the end-binding events of MCAK, we wondered how MCAK could recognize the end of dynamic microtubules. Previous studies, mostly based on stabilized microtubules, proposed the idea that MCAK binds to microtubule ends by recognizing curved protofilaments (Asenjo et al., 2013; Benoit et al., 2018; Trofimova et al., 2018). This model predicts that the binding site of MCAK is located to the distalmost tip of growing microtubule ends, where the XMAP215 family members are thought to bind (i.e. the distalmost cap) (Ayaz et al., 2012; Brouhard et al., 2008). We tested this prediction by measuring the end-binding regions of MCAK, EB1 and XMAP215 (**Fig. 2A**). To our surprise, the binding region of MCAK was longer than that of XMAP215. It extended proximally towards the lattice, and covered the binding region of EB1 (i.e. the EB cap) (Maurer et al., 2012). To further understand if MCAK binds to the distalmost cap and the EB cap with different kinetics, we compared the dwell time of the distally located MCAK to that of the proxi-

183 mally distributed ones (**Fig. 2B**). Note that we defined the MCAK molecules localiz-
184 ing to the left of the FWHM of XMAP215 binding region as the proximally distribut-
185 ed, while those localizing to the right of the FWHM of EB1 binding region was dis-
186 tally distributed. No significant difference was found (τ_{distal}=0.8 ± 0.5, n=28 binding
187 events; $\tau_{proximal}$=0.7±0.6, n=45 binding events; p>0.3, the two-tailed Mann-Whitney U
188 test with Bonferroni correction). Note that in all experiments, the morphologies of
189 growing microtubule ends were comparable (**Fig. 2C**). Based on these results, we
190 conclude that MCAK recognizes the entire GTP-cap. This result is intriguing as it
191 suggests that in addition to the curved protofilaments, there are additional end-binding
192 sites for MCAK. Moreover, this also provides an independent measurement for the
193 size of the GTP cap at growing microtubule ends, which was previously determined
194 using the tubulin dilution experiments or by measuring the binding region of EB1
195 (Duellberg et al., 2016).

196 **MCAK strongly binds to GTPγS microtubules in a nucleotide-independent**
197 **manner**

198 How could MCAK bind to the EB cap? The tubulin dimers in the EB cap are
199 thought to be different from those in the distalmost cap (Maurer et al., 2011). For
200 example, the distalmost tubulin dimers (mostly GTP-tubulin) often lack lateral con-
201 strains (Vitre et al., 2008) and adopt a bent shape (Hoeoeg et al., 2011; McIntosh et al.,
202 2018), while those in the EB cap (mostly GDP·Pi-tubulin) have formed at least some
203 lateral contacts and had a more straight conformation (Guesdon et al., 2016; Maurer et
204 al., 2012). To address this issue, we first examined that to what extent, MCAK may
205 adopt a similar end-binding mechanism as EB1.

206 We tested the contribution of GDP·Pi-tubulins, which underlies the end-binding
207 preference of EBs (Maurer et al., 2011; Maurer et al., 2012). Here, we compared the
208 binding affinity of MCAK·AMPPNP on GTPγS, GMPCPP and GDP microtubules
209 (**Fig. 3A**), which mimics tubulin dimers in different GTP hydrolysis states. Because
210 MCAK in the concentration required for a full-lattice decoration would rapidly disas-
211 semble microtubules, we cannot directly compare the total binding of MCAK on mi-
212 crotubules as what was previously done for the EBs (Maurer et al., 2011; Maurer et al.,
213 2012). Therefore, we took an alternative approach by recording the single-molecule
214 binding of MCAK·AMPPNP (1 nM) on microtubules and measuring fluorescence in-
215 tensity summation over a period of time (1000 frames, 0.3 s per frame) (**Fig. s2**).
216 Strikingly, we found that MCAK·AMPPNP bound strongly to GTPγS microtubules
217 (**Fig. 3 A-C**). Quantitative analysis revealed a significantly stronger binding on
218 GTPγS microtubules than on GMPCPP or GDP microtubules (**Fig. 3 B-C**). Because
219 the tubulin dimers in GTPγS microtubules were found to be the analogue of
220 GDP·Pi-tubulins (Maurer et al., 2011), this result suggests that MCAK·ATP has a
221 binding preference for GDP·Pi-tubulins.

222 Because the end-binding affinity and preference of MCAK depends on the nu-
223 cleotide state, we wondered if the preference for GTPγS microtubules is similar.

Therefore, we performed the same experiments using MCAK·AMPPNP, MCAK·ATP, MCAK·ADP and MCAK·APO. Although the MCAK variants bound to microtubules with different affinities (MCAK·APO > MCAK·AMPPNP > MCAK·ADP > MCAK·ATP) (**Fig. 3B**), they all showed a clear binding preference for GTPγS microtubules over GDP or GMPCPP microtubules (**Fig. 3 B-C**). These observations suggest that the binding preference to GTPγS microtubules (i.e. GDP·Pi-tubulin) is, to a large extent, independent on the nucleotide state of MCAK.

MCAK binds to the end region of stabilized GMPCPP microtubules in a nucleotide state-dependent manner

We noted that MCAK showed a nucleotide state-dependence in the binding preference for dynamic microtubule ends, but the binding to GTPγS microtubules is nucleotide independent. Therefore, we wondered if the binding to curved protofilaments at the distalmost cap of dynamic microtubules could account for the nucleotide-state dependence. To address this issue, we measured the binding preference of MCAK at the end of stabilized GMPCPP microtubules (**Fig. 4A**), where the length and curvature of protofilaments are thought to be similar to those at the end of dynamic microtubules but has no GDP·Pi-tubulins (Manka and Moores, 2018; McIntosh et al., 2018). We found that the MCAK in ATP or AMPCPP state showed a binding preference for the end of GMPCPP microtubules, while MCAK·ADP and MCAK·APO did not (**Fig. 4B-C**). This is similar to the observation that MCAK·ADP and MCAK·APO had a lower binding preference for dynamic microtubule ends, thereby providing an explanation for the nucleotide state-dependence of the end-binding of MCAK.

The binding preference for GDP·Pi-tubulins facilitates the end-binding of MCAK

Intuitively, the binding preference for the EB cap, in addition to the previously established preference for the curved protofilaments, would provide more high-affinity sites for MCAK, thereby facilitating the end-binding of MCAK. To tested this idea, we studied two mutants, $MCAK^{K524A}$ (K524A in the α4 helix) and $MCAK^{V298S}$ (V298S in the L2 loop). The α4 helix of MCAK interacts with the intra-dimeric interface of tubulin heterodimer (**Fig. 5A**), and the K524A mutation is expected to disrupt the electrostatic interaction between MCAK and tubulin heterodimer (Patel et al., 2016; Wang et al., 2017). The L2 loop of MCAK has a direct contact with the inter-dimeric interface of tubulin heterodimer (**Fig. 5A**), and the V298S mutation is expected to disrupt the hydrophobic interaction between the L2 loop and α-tubulin (Wang et al., 2015). We confirmed that both mutants were depolymerization-deficient (**Fig. s3**), as previously reported (Wang et al., 2017; Wang et al., 2015).

Compared to MCAK, $MCAK^{K524A}$ showed a significantly reduced binding intensity on microtubules. Meanwhile, it still showed a binding preference for GTPγS microtubules (**Fig. 5B-C**), but the ratios between the binding intensity on GTPγS microtubules and that on GMPCPP or GDP microtubules were both reduced (**Fig. 5D**). This suggests that $MCAK^{K524A}$ had a lower preference for GTPγS microtubules. On the

contrary, we found that MCAK^{K524A} showed a higher binding to the end than to the lattice of GMPCPP microtubules (**Fig. 5 E-F**), suggesting that the binding preference for curved protofilament is maintained. Therefore, MCAK^{K524A} could be a candidate variant to test how the preference for GDP·Pi-tubulin contributes to the end-binding preference of MCAK. We found that MCAK^{K524A} could bind to dynamic microtubule ends, but its $k_{on\text{-}P}$ and $R_{E/L}$ were both reduced (**Fig. 5 G-H**). Meanwhile, the end-binding dwell time of MCAK^{K524A} was also reduced (**Fig. 5I**), suggesting a higher off-rate. These results are consistent with the idea that the higher binding affinity to GDP·Pi-tubulin directly contributes to the end-binding preference of MCAK at growing microtubule ends.

By comparison, the binding preferences of MCAK^{V298S} for GTPγS microtubules and the end of GMPCPP microtubules were both reduced (**Fig. 5 B-F**), implying the reduced preferences for both the EB cap and the distalmost cap. In the dynamics assay, the $k_{on\text{-}P}$, $R_{E/L}$ and dwell time of MCAK^{V298S} were decreased in comparison to those of MCAK (**Fig. 5 H-I**). We noted that the $k_{on\text{-}P}$, $R_{E/L}$ and dwell time of MCAK^{V298S} were similar to those of MCAK^{K524A} (two-tailed Mann-Whitney U test with Bonferroni correction, $p>0.05$), suggesting that the binding to the EB cap makes a major importance for the end-binding preference of MCAK at dynamic microtubule ends.

Functional specification of MCAK and XMAP215

Having revealed the novel binding sites of MCAK in dynamic microtubule ends, we wondered how MCAK may work in coordination with other microtubule plus tip-binding proteins, for example EB1 and XMAP215. It has been shown that EB1 interacts with and recruits MCAK to growing microtubule ends (Gouveia et al., 2010; Honnappa et al., 2009; Lee et al., 2008), so it is straightforward that EB1 would facilitate the function of MCAK as a catastrophe factor. On the contrary, MCAK and XMAP215 were shown to antagonistically regulate the assembly of microtubules, and it was thought that these two molecules may compete directly for the growing ends (Tournebize et al., 2000). Here, we showed that the binding regions of MCAK and XMAP215 in growing microtubule ends are partially overlapping. In addition, previously resolved structural models suggest that MCAK and XMAP215 likely bind to similar regions on tubulin dimers (**Fig. s4**). Therefore, these two molecules could indeed compete for the binding sites in the distalmost cap. However, it is not yet clear to what extent, the competition from XMAP215 would antagonize the function of MCAK, especially given the recent finding that XMAP215 itself could promote the catastrophe of microtubules (Farmer et al., 2021). Therefore, it is intriguing what would be the collective effect of MCAK and XMAP215.

To address this issue, we studied how they together regulate microtubule grow rate and catastrophe frequency. Based on our pilot experiments, we chose 20 nM for MCAK and 50 nM for XMAP215 as the representative concentrations. In the presence of 20 nM MCAK, the dynamic microtubules could grow but showed a significantly increased catastrophe frequency and shorter lifetime (**Fig. 6 A-B**). Meanwhile,

50 nM XMAP215 increased growth rate by more than four times (control: 0.8 ± 0.1 μm min^{-1}, n=97 microtubules from 6 assays; 50 nM XMAP215: 3.7 ± 0.4 μm min^{-1}, n=50 microtubules from 3 assays). We noted that XMAP215 alone caused a mild shortening in the lifetime of dynamic microtubules (**Fig. 6 A-B**). This is consistent with the previous report and suggesting the enhanced fluctuations in the end structures (Farmer et al., 2021). We then added both 20 nM MCAK and 50 nM XMAP215. In this case, microtubule grew in a similar rate as if there was no MCAK (3.9 ± 0.4 μm min^{-1}, n=52 microtubules from 3 assays, p=0.5, the two-tailed Mann-Whitney U test with Bonferroni correction), suggesting that MCAK has no major effect on the function of XMAP215 as a polymerase. Meanwhile, the lifetime of dynamic microtubules became shorter than that with only MCAK or XMAP215 (**Fig. 6B**). To understand if this reflects the simple summation of the separate contributions of MCAK and XMAP215 or their synergistic effect, we calculated the probability-based catastrophe frequency in all conditions (**Fig. 6C**) (Gardner et al., 2011).We found that the effects of MCAK and XMAP215 on the probability of microtubule catastrophe were only additive, showing that there was no synergic effect in regulating catastrophe frequency (**Fig. 6C**).

Discussion

This study provides mechanistic insights into understanding the end-binding mechanism of MCAK. The previously established view on the end-binding mechanism of MCAK is based on specific recognition of curved protofilaments at the distalmost tip of growing microtubules (Asenjo et al., 2013; Benoit et al., 2018; Tan et al., 2008). The findings in the present study add to the model by showing that MCAK strongly binds to the EB cap, and this binding preference could facilitate the end-binding and in turn the depolymerizing activity of MCAK. We now discuss our main findings and their implications.

MCAK preferentially binds to the GDP·Pi-tubulin in a nucleotide state-independent manner

Our main finding is that MCAK preferentially binds to the EB cap where the GDP·Pi-tubulins gather, in addition to the previously known binding preference for the curved protofilaments (Asenjo et al., 2013; Benoit et al., 2018; Tan et al., 2008). This conclusion is based on several lines of evidence. First, MCAK·ADP or MCAK·APO shows a significant reduction but not a complete loss in the binding preference for dynamic microtubule ends. However, their binding preference for stabilized microtubule ends is completely absent. The different binding behavior to dynamic and stabilized microtubule ends suggests that other end features, in addition to the curved protofilament, also contribute to the end-binding of MCAK. Second, the localization analysis of MCAK shows that MCAK binds to the entire GTP cap, including the EB cap and the distalmost cap. Third, MCAK shows a binding preference for GTPγS microtubules over GDP or GMPCPP microtubules. Because the tubulin in GTPγS microtubules is considered to be the analogues to the GDP·Pi-tubulins (Maurer et al., 2011; Maurer et al., 2012), MCAK is expected to have a high affinity to the EB cap. Fourth, the loss of the binding preference of $MCAK^{K524A}$ for GTPγS microtubules, but not for the ends of GMPCPP microtubules, suggests that the binding preference for GDP·Pi-tubulins is required for the optimal end-binding affinity and preference.

Implications for the working mechanism of MCAK

We think that our findings add to the current working model of MCAK in four aspects. First, the nucleotide state-independent binding preference for GDP·Pi-tubulins provides a mechanism for MCAK staying bound to the GTP cap after ATP hydrolysis. For example, in a speculative scenario (**Fig. 7A**), when one of the motor domains of MCAK is converted to the ADP or APO state after the breakage of the terminal tubulin dimers, it loses the binding affinity to the curved protofilaments (**Fig. 7A**). However, it still preferentially binds to GDP·Pi-tubulins, so it has a larger chance binding back to the EB cap than to the lattice and thereby remains within the GTP cap (**Fig. 7A**). Then, while the ADP is being replaced by a new ATP, this motor domain could diffuse around to explore the working site for the next round of catalysis. In this way, the nucleotide state-independent binding feature of MCAK would fa-

364 cilitate the binding to the dynamic microtubule ends. This idea is consistent with the
365 findings that $MCAK^{K524A}$, a mutant showing reduced preference for GDP·Pi-tubulins,
366 had disrupted end-binding affinity, preference and dwell time.

367 Second, the previous studies showed that MCAK has a direct interaction with
368 EB1, and EB1 increases the end-binding rate of MCAK (Gouveia et al., 2010;
369 Honnappa et al., 2009; Lee et al., 2008). Intuitively, there is a gap here that after the
370 arrival of MCAK at the binding region of EB1, how it could reach the high-affinity
371 binding site or working site, previously known as the curved protofilament at the dis-
372 talmost tip (Asenjo et al., 2013; Benoit et al., 2018; Tan et al., 2008). Our finding fills
373 this gap by showing that MCAK also binds strongly to the GDP·Pi-tubulins where the
374 EBs bind (**Fig. 7B**). Moreover, MCAK could explore the entire length of GTP cap
375 (~160 nm) by 1D lattice diffusion within the binding dwell time. In this way, we argue
376 that MCAK could find the precisely catalyzing site at dynamic microtubule ends by a
377 combination of 3D diffusion (to first reach the GTP cap) and 1D lattice diffusion
378 (short range, within the GTP cap).

379 Third, a previous study showed that the association on-rate is an important regu-
380 lated parameter for the functions of MCAK (Cooper et al., 2010). The binding affinity
381 and preference for the EB cap, in addition to the distalmost cap, would intuitively
382 provide more binding sites, thereby further increasing the binding on-rate of MCAK.
383 This idea is also consistent with the finding that $MCAK^{K524A}$, a mutant with a reduced
384 preference for GDP·Pi-tubulins, had a reduced end-binding on-rate.

385 Fourth, despite having partially overlapped binding regions, MCAK and
386 XMAP215 provide independent controls for catastrophe frequency and growth rate of
387 microtubules, respectively (**Fig. 7B**). The free combination of these two regulators
388 suggests a straightforward strategy in the regulations on the length and mass of mi-
389 crotubules, i.e., simply by controlling their amount (i.e. expression level) or activity
390 (e.g. via phosphorylation). In this sense, the working scenario of MCAK and
391 XMAP215 provides a molecular paradigm to understand how the regulators of mi-
392 crotubules orchestrate their behaviors at the nanoscopic end structure of dynamic mi-
393 crotubules and reflects a clear logic in the regulatory network of microtubule dynam-
394 ics.

Materials and Methods

Protein expression and purification

MCAK purification.

GFP-MCAK was expressed using a modified BAC-to-BAC protocol. The purification was performed as previously described (Helenius et al., 2006). Briefly, the cells were lysed by dounce homogenization in the lysis buffer. The lysate was centrifuged at 40,000 rpm for 60 min at 4°C (XPN-100 ultracentrifuge, Type 45 Ti rotor, Beckman, USA). The supernatant was filtered through a 0.45 μm filter (Pall, 66229) and then purified using a cation-exchange column (HiTrap SP-HP, Cat.17115101, GE, USA). The protein was eluted using the elution buffer supplemented with a continuous salt gradient (0.15~1.0 M NaCl). The peak fractions were pooled together and then loaded onto a Ni-sepharose column (QIAGEN, 30210). The column was then washed with the washing buffer I. After the washing step, 3C Protease (final concentration 10 μg/ml) (Thermo Fisher Scientific, 88946) was used to perform on-column his-tag cleavage overnight at 4°C. The eluate was further purified using a gel-filtration column (Superdex 200 increase 10/300 GL column, Cat. 28990944, GE, USA) and eluted using the washing buffer II. The purified MCAK was frozen in liquid N_2 and stored at -80°C. Lysis buffer: 50 mM HEPES pH 7.5, 150 mM NaCl, 5% glycerol, 0.1% Tween 20, 1.5 mM $MgCl_2$, 3 mM EGTA, 1 mM DTT, 0.5 mM Mg-ATP, 10 units/ml Benzonase. Elution buffer: 6.7 mM HEPES pH 7.5, 6.7 mM MES, 6.7 mM sodium acetate, 1.5 mM $MgCl_2$, 10 μM Mg-ATP. Washing buffer I: 50 mM $NaPO_4$ buffer pH 7.5, 300 mM NaCl, 10 mM imidazole, 10% glycerol, 1 mM $MgCl_2$, 10 μM Mg-ATP. Washing buffer II: BRB80, 300 mM KCl, 1 mM DTT and 10 μM Mg-ATP. BRB80: 80 mM PIPES/KOH pH 6.9, 1 mM $MgCl_2$, 1 mM EGTA.

EB1 purification.

EB1-GFP was expressed and purified as previously described (Song et al., 2020). Briefly, EB1-GFP was expressed in the *BL21 E. coli* strain and lysed using sonication in the lysis buffer. The lysate was centrifuged at 40,000 rpm for 60 min at 4°C. The supernatant was filtered through a 0.45 μm filter and loaded onto a Ni-sepharose column. The column was then washed using the washing buffer. After the washing step, 3C Protease (final concentration 10 μg/ml) was used to perform on-column his-tag cleavage overnight at 4°C. The eluate was desalted into the storage buffer using the PD-10 desalting column (GE, 17085101). The final purified protein was frozen in liquid N_2 and stored at -80 °C. Lysis buffer: 50 mM $NaPO_4$ buffer pH 7.5, 300 mM NaCl, 10% glycerol, 10 mM imidazole, 1 mM DTT, 0.1% Tween 20. Washing buffer: 50 mM $NaPO_4$ buffer pH 7.5, 300 mM NaCl, 10% glycerol, 30 mM imidazole, 1 mM DTT. Storage buffer: BRB80, 100 mM KCl, 10% glycerol and 1 mM DTT.

XMAP215 purification.

XMAP215-GFP was expressed using a modified BAC-to-BAC protocol. The purification was performed as previously described (Brouhard et al., 2008). Briefly, the

435 cells were lysed by dounce homogenization in the lysis buffer. The lysate was centri-
436 fuged at 40,000 rpm for 60 min at 4°C. The supernatant was filtered through a 0.45
437 μm filter and then purified using a cation-exchange column. The protein was eluted
438 using the elution buffer supplemented with a continuous salt gradient (0.15~1.0 M
439 NaCl). The peak fractions were pooled together and then loaded onto a Ni-sepharose
440 column. The column was then washed with the washing buffer I. The protein was
441 eluted using the washing buffer I supplemented with a continuous imidazole gradient
442 (20-300 mM). The fractions with best purity were pooled together and further purified
443 using a gel-filtration column (Superdex 200 increase 10/300 GL column, Cat.
444 28990944, GE, USA) and eluted using the washing buffer II. The final purified
445 XMAP215 was frozen in liquid N_2 and stored at -80°C. Lysis buffer: 50 mM HEPES
446 pH 7.5, 50 mM NaCl, 5% glycerol, 0.1% Tween 20, 1 mM DTT, 10 units/ml Benzo-
447 nase. Elution buffer: 6.7 mM HEPES pH 7.5, 6.7 mM MES, 6.7 mM sodium acetate.
448 Washing buffer I: 50 mM NaPO4 buffer pH 7.5, 300 mM NaCl, 10 mM imidazole, 10%
449 glycerol, 1 mM $MgCl_2$, 10 μM Mg-ATP. Washing buffer II: BRB80, 150 mM KCl, 1
450 mM DTT.

451 *Tubulin preparation.*

452 Tubulin was purified from porcine brain tissues by two cycles of polymerization
453 and depolymerization followed by affinity purification using the TOG-based column,
454 as previously described (Gell et al., 2010; Widlund et al., 2012). Tubulin was labeled
455 with biotin (Thermo Fisher Scientific, 20217), TAMRA (Thermo Fisher Scientific,
456 C1171) and Alexa Fluor 647 (Thermo Fisher Scientific, A20106) using the NHS es-
457 ters according to the standard protocols (Gell et al., 2010).

458 **Microtubule depolymerization assay**

459 Microtubules (5% Alexa Fluor 647 labeled and 20% biotin labeled) were pol-
460 ymerized in the presence of GMPCPP (JenaBioscience, NU-405L) as previously de-
461 scribed (Song et al., 2020). The GMPCPP-stabilized microtubules were immobilized
462 on the surface of a cover glass using the biotin-NeutrAvidin protein links (Thermo
463 Fisher Scientific, 31000). GFP-MCAK was then added into the flow cell in the imag-
464 ing buffer. The sample was kept at 35°C using a temperature controller (Tokai Hit,
465 Japan). Images were recorded using a total internal reflection microscope (TIRFM)
466 (Olympus, Japan) equipped with a 100× 1.49 N.A. oil TIRF objective (Olympus, Ja-
467 pan) and an Andor 897 Ultra EMCCD camera (Andor, Belfast, UK). Images were
468 recorded every 5 s with a 100 ms exposure. Imaging buffer: BRB80 supplemented
469 with 1 mM ATP, 50 mM KCl, 80 mM D-glucose, 0.4 mg/ml glucose oxidase, 0.2
470 mg/ml catalase, 0.8 mg/ml casein, 1% β-mercaptoethanol, 0.001% Tween 20.

471 **Microtubule dynamics assay**

472 Microtubule dynamics assay was performed as previously described (Song et al.,
473 2020). Briefly, the immobilized GMPCPP-stabilized microtubules were used as the
474 template for microtubule growth. Tubulin dimers (13% TAMRA labeled) and the

475 protein of interest were then added into the flow cell in the imaging buffer. The sam-
476 ple was kept at 35°C using a temperature controller (Tokai Hit, Japan). Images were
477 recorded using a TIRFM (Olympus, Japan). To record microtubule dynamics, images
478 were recorded every 5 s with a 100 ms exposure. To record single molecule binding
479 events, images were recorded every 100 ms with a 50 ms exposure. Imaging buffer:
480 BRB80 supplemented with 1 mM ATP, 2 mM GTP, 50 mM KCl, 0.15% sodium car-
481 boxymethylcellulose, 80 mM D-glucose, 0.4 mg/ml glucose oxidase, 0.2 mg/ml cata-
482 lase, 0.8 mg/ml casein, 1% β-mercaptoethanol, 0.001% Tween 20.

483 **The diffusion coefficient of MCAK on dynamic microtubule lattices**

484 The diffusion coefficient of MCAK on dynamic microtubule lattices was calcu-
485 lated as previously described (Helenius et al., 2006). Firstly, we gained the position
486 coordinates of MCAK at its molecular trajectory on dynamic microtubule lattices us-
487 ing the plugin of imageJ (Fiji), TrackMate (Tinevez et al., 2017). Note that the mini-
488 mum track length was kept at 400 ms (100 ms/frame). Then, the mean-squared dis-
489 placement (MSD) of MCAK at every molecular trajectory (203 trajectories from 3
490 assays) was calculated against the interval (100 ms/frame) by an in-house script of
491 MATLAB. Lastly, the MSDs of MCAK was plotted against the time interval, and the
492 diffusion coefficient, D was obtained by a linear regression analysis ($\langle x^2 \rangle = 2Dt$) in
493 Origin 8.0 (OriginLab Corporation, USA).

494 **The flux of MCAK reaching growing microtubule ends**

495 The calculation of the flux of MCAK reaching growing microtubule ends by
496 one-dimensional lattice-diffusion was performed according to Fick's first equation of
497 diffusion (Helenius et al., 2006):

498 $$J = -D \cdot \partial c / \partial x \quad \text{(Eq.1)}$$

499 where J is the flux of MCAK reaching growing microtubule ends, $c(x,t)$ is the con-
500 centration of MCAK on microtubule lattice at position x from the growing microtu-
501 bule end and time t.

502 $$\text{When } x = 0 \quad J_0 = -D \cdot c_\infty / x_0 \quad \text{(Eq. 2)}$$

503 Where

504 $$x_0 = (D/k_{\text{off}})^{1/2}$$

$$c(x \to \infty) = c_\infty = k_{\text{on}} \cdot C / k_{\text{off}}$$

505 Where C is the concentration of MCAK. Therefore, we can calculate the flux by tak-
506 ing the measured parameters (D, k_{on}, C and k_{off}) into the equation.

507 **Localization analysis at growing microtubule ends**

The analysis on the single-molecule localization at growing microtubule ends was performed as previously described (Song et al., 2020). Briefly, we determined the position of growing microtubule end by considering the microtubule lattice as a Gaussian wall and its end as a half-Gaussian. This model was used to fit the microtubule end and determined the position of microtubule end in every frame. The peak position of the half-Gaussian was used as the origin of the positional axis, which was used as a reference to measure the localization of individual single-molecule binding events. We estimated that the accuracy of microtubule end tracking was ~6 nm by measuring standard error of the distribution of the estimated error in microtubule end position (Demchouk et al., 2011). To measure the precise localization of individual binding events at growing microtubule ends, a Gaussian function was used to fit the intensity profile of individual molecules. We estimated that the accuracy of the measured position was ~2 nm by measuring standard error of the fitting peak location (Maurer et al., 2014). The peak location was recorded as the position of each molecule in every frame. The average peak location over the entire binding period was recorded as the position of the molecule. The positional distributions of GFP-MCAK, EB1-GFP, XMAP215-GFP at growing microtubule ends were plotted along the longitudinal axis of microtubule. Finally, the plots of GFP-MCAK and XMAP215-GFP were fitted to a Gaussian function and the plots of EB1-GFP was fitted to an exponentially modified Gaussian function, from which we calculated the FWHM as an estimation for the length of the binding region of each molecule.

Microtubule polymerization

GMPCPP, GDP and GTPγS microtubules were polymerized as previously described (Manka and Moores, 2018). Briefly, GMCPP-microtubules were polymerized using a mixture of 10 μM tubulin, 1 mM GMPCPP (JenaBioscience, NU-405L) and 4 mM $MgCl_2$ in BRB80, which was incubated for 2 hr at 37˚C. The polymerized microtubules were then collected using an Air-Driven Ultracentrifuge (Beckman, 340401), which were then resuspended in BRB80 and stored at 37˚C. GDP-microtubules were polymerized using a mixture of 40 μM tubulin, 1 mM GTP (Roche, 10106399001), 4 mM $MgCl_2$ and 4% DMSO (Sigma, 276855). The mixture was incubated for 30 min at 37˚C. The polymerized microtubules were collected using an Air-Driven Ultracentrifuge, resuspended in BRB80 with 20 μM taxol (Cell Signaling Technology, 9807) and stored at 37˚C. GTPγS microtubules were obtained using two rounds of polymerizations. In the first round, a mixture of 40 μM tubulin, 2 mM GTPγS (Roche, 10220647001) and 4 mM $MgCl_2$ in BRB80 was incubated for 5 hours at 37°C. In the second round, 5 μl of the product from the first polymerization was mixed with additional 40 μM tubulin, 2 mM GTPγS and 4 mM $MgCl_2$ to make a final 25 μl reaction mixture. This mixture was incubated overnight at 37°C to obtain long GTPγS microtubules. The polymerized microtubules were collected using an Air-Driven Ultracentrifuge, resuspended in BRB80 with 20 μM taxol and stored at 37˚C.

MCAK binding to different microtubules

550 Different nucleotide microtubules were first immobilized in flow cells.
551 GFP-MCAK or its mutants were then added into the flow cell in the imaging buffer.
552 Images were recorded every 300 ms with a 100 ms exposure. Imaging buffer: BRB80
553 supplemented with 1 mM ATP, ADP or AMPCPP, 20 μM taxol, 50 mM KCl, 80 mM
554 D-glucose, 0.4 mg/ml glucose oxidase, 0.2 mg/ml catalase, 0.8 mg/ml casein, 1%
555 β-mercaptoethanol, 0.001% Tween 20.

556 **The binding intensity of GFP-MCAK on GMPCPP microtubule ends**

557 To measure the binding intensity of GFP-MCAK on GMPCPP microtubule ends,
558 an intensity profile of GFP-MCAK or the GMPCPP microtubule was plotted along the
559 microtubule. The average binding intensity of GFP-MCAK of two pixels represents
560 the end-binding intensity of GFP-MCAK at the corresponding position of the end, to
561 the lattice from the midpoint of the microtubule intensity attenuation at the microtu-
562 bule end.

563 **Gamma fitting of microtubule lifetimes and catastrophe frequency analysis**

564 The lifetime data of dynamic microtubules were fitted to the gamma density
565 function using the dfittool toolbox in the MATLAB (Mathworks, USA). The probabil-
566 ity-based catastrophe frequency is calculated as the ratio of the number of catastrophe
567 events observed at a certain lifetime to the total number of microtubules that reached
568 this lifetime (Gardner et al., 2011).

Acknowledgement

The authors thank Pengpeng Yu (school of life sciences and technology, TongJi University), Chunguang Wang (school of life sciences and technology, TongJi University), Peng Shi (school of basic medical sciences, Peking University) and Congying Wu (school of basic medical sciences, Peking University) for technical assistance. Special thanks to the light microscopy and protein facility in Tsinghua University. We acknowledge our funding from National Natural Sciences Foundation of China (32070704, 32370730) and IDG/McGovern Institute for Brain Research (Tsinghua University).

References

Aizawa, H., Y. Sekine, R. Takemura, Z.Z. Zhang, M. Nangaku, and N. Hirokawa. 1992. KINESIN FAMILY IN MURINE CENTRAL-NERVOUS-SYSTEM. *Journal of Cell Biology*. 119:1287-1296.

Alberts, B. 2015. Molecular biology of the cell.

Asenjo, A.B., C. Chatterjee, D. Tan, V. DePaoli, W.J. Rice, R. Diaz-Avalos, M. Silvestry, and H. Sosa. 2013. Structural Model for Tubulin Recognition and Deformation by Kinesin-13 Microtubule Depolymerases. *Cell Reports*. 3:759-768.

Ayaz, P., X. Ye, P. Huddleston, C.A. Brautigam, and L.M. Rice. 2012. A TOG:alpha beta-tubulin Complex Structure Reveals Conformation-Based Mechanisms for a Microtubule Polymerase. *Science*. 337:857-860.

Benoit, M.P.M.H., A.B. Asenjo, and H. Sosa. 2018. Cryo-EM reveals the structural basis of microtubule depolymerization by kinesin-13s. *Nature Communications*. 9.

Brouhard, G.J., J.H. Stear, T.L. Noetzel, J. Al-Bassam, K. Kinoshita, S.C. Harrison, J. Howard, and A.A. Hyman. 2008. XMAP215 is a processive microtubule polymerase. *Cell*. 132:79-88.

Cooper, J.R., M. Wagenbach, C.L. Asbury, and L. Wordeman. 2010. Catalysis of the microtubule on-rate is the major parameter regulating the depolymerase activity of MCAK. *Nature Structural & Molecular Biology*. 17:77-U98.

Demchouk, A.O., M.K. Gardner, and D.J. Odde. 2011. Microtubule Tip Tracking and Tip Structures at the Nanometer Scale Using Digital Fluorescence Microscopy. *Cellular and Molecular Bioengineering*. 4:192-204.

Desai, A., S. Verma, T.J. Mitchison, and C.E. Walczak. 1999. Kin I kinesins are microtubule-destabilizing enzymes. *Cell*. 96:69-78.

Duellberg, C., N.I. Cade, D. Holmes, and T. Surrey. 2016. The size of the EB cap determines instantaneous microtubule stability. *eLife*. 5:23.

Farmer, V., G. Arpa, S.L. Hall, and M. Zanic. 2021. XMAP215 promotes microtubule catastrophe by disrupting the growing microtubule end. *Journal of Cell Biology*. 220.

Gardner, M.K., M. Zanic, C. Gell, V. Bormuth, and J. Howard. 2011. Depolymerizing Kinesins Kip3 and MCAK Shape Cellular Microtubule Architecture by Differential Control of Catastrophe. *Cell*. 147:1092-1103.

Gell, C., V. Bormuth, G.J. Brouhard, D.N. Cohen, S. Diez, C.T. Friel, J. Helenius, B. Nitzsche, H. Petzold, J. Ribbe, E. Schaeffer, J.H. Stear, A. Trushko, V. Varga, P.O. Widlund, M. Zanic, and J. Howard. 2010. Microtubule Dynamics Reconstituted In Vitro and Imaged by Single-Molecule Fluorescence Microscopy. *In* Microtubules, in Vitro: Microtubules, in Vitro. Vol. 95. L. Wilson and J.J. Correia, editors. 221-245.

Ghosh-Roy, A., A. Goncharov, Y. Jin, and A.D. Chisholm. 2012. Kinesin-13 and Tubulin Posttranslational Modifications Regulate Microtubule Growth in Axon Regeneration. *Dev. Cell*. 23:716-728.

Gouveia, S.M., K. Leslie, L.C. Kapitein, R.M. Buey, I. Grigoriev, M. Wagenbach, I. Smal, E. Meijering, C.C. Hoogenraad, L. Wordeman, M.O. Steinmetz, and A. Akhmanova. 2010. In Vitro Reconstitution of the Functional Interplay between MCAK and EB3 at Microtubule Plus Ends. *Curr. Biol.* 20:1717-1722.

Guesdon, A., F. Bazilel, R.M. Buey, R. Mohan, S. Monier, R.R. Garcia, M. Angevin, C. Heichette, R.

Wieneke, R. Tampe, L. Duchesne, A. Akhmanova, M.O. Steinmetz, and D. Chretien. 2016. EB1 interacts with outwardly curved and straight regions of the microtubule lattice. *Nature Cell Biology*. 18:1102-1108.

Helenius, J., G. Brouhard, Y. Kalaidzidis, S. Diez, and J. Howard. 2006. The depolymerizing kinesin MCAK uses lattice diffusion to rapidly target microtubule ends. *Nature*. 441:115-119.

Hoeoeg, J.L., S.M. Huisman, Z. Seboe-Lemke, L. Sandblad, J.R. McIntosh, C. Antony, and D. Brunner. 2011. Electron tomography reveals a flared morphology on growing microtubule ends. *Journal of Cell Science*. 124:693-698.

Honnappa, S., S.M. Gouveia, A. Weisbrich, F.F. Damberger, N.S. Bhavesh, H. Jawhari, I. Grigoriev, F.J.A. van Rijssel, R.M. Buey, A. Lawera, I. Jelesarov, F.K. Winkler, K. Wuethrich, A. Akhmanova, and M.O. Steinmetz. 2009. An EB1-Binding Motif Acts as a Microtubule Tip Localization Signal. *Cell*. 138:366-376.

Hunter, A.W., M. Caplow, D.L. Coy, W.O. Hancock, S. Diez, L. Wordeman, and J. Howard. 2003. The kinesin-related protein MCAK is a microtubule depolymerase that forms an ATP-hydrolyzing complex at microtubule ends. *Molecular Cell*. 11:445-457.

Janke, C., and M.M. Magiera. 2020. The tubulin code and its role in controlling microtubule properties and functions. *Nature Reviews Molecular Cell Biology* 21:307-326.

Kapitein, L.C., and C.C. Hoogenraad. 2015. Building the Neuronal Microtubule Cytoskeleton. *Neuron*. 87:492-506.

Kline-Smith, S.L., A. Khodjakov, P. Hergert, and C.E. Walczak. 2004. Depletion of centromeric MCAK leads to chromosome congression and segregation defects due to improper kinetochore attachments. *Molecular Biology of the Cell*. 15:1146-1159.

Lee, T., K.J. Langford, J.M. Askham, A. Bruning-Richardson, and E.E. Morrison. 2008. MCAK associates with EB1. *Oncogene*. 27:2494-2500.

Manka, S.W., and C.A. Moores. 2018. The role of tubulin-tubulin lattice contacts in the mechanism of microtubule dynamic instability. *Nature Structural & Molecular Biology*. 25:607-+.

Maurer, S.P., P. Bieling, J. Cope, A. Hoenger, and T. Surrey. 2011. GTP gamma S microtubules mimic the growing microtubule end structure recognized by end-binding proteins (EBs). *Proceedings of the National Academy of Sciences of the United States of America*. 108:3988-3993.

Maurer, S.P., N.I. Cade, G. Bohner, N. Gustafsson, E. Boutant, and T. Surrey. 2014. EB1 Accelerates Two Conformational Transitions Important for Microtubule Maturation and Dynamics. *Curr. Biol.* 24:372-384.

Maurer, S.P., F.J. Fourniol, G. Bohner, C.A. Moores, and T. Surrey. 2012. EBs Recognize a Nucleotide-Dependent Structural Cap at Growing Microtubule Ends. *Cell*. 149:371-382.

McIntosh, J.R., E. O'Toole, G. Morgan, J. Austin, E. Ulyanov, F. Ataullakhanov, and N. Gudimchuk. 2018. Microtubules grow by the addition of bent guanosine triphosphate tubulin to the tips of curved protofilaments. *Journal of Cell Biology*. 217:2691-2708.

Moores, C.A., and R.A. Milligan. 2006. Lucky 13 - microtubule depolymerisation by kinesin-13 motors. *Journal of Cell Science*. 119:3905-3913.

Noda, Y., R. Satoyoshitake, S. Kondo, M. Nangaku, and N. Hirokawa. 1995. KIF2 IS A NEW MICROTUBULE-BASED ANTEROGRADE MOTOR THAT TRANSPORTS MEMBRANOUS ORGANELLES DISTINCT FROM THOSE CARRIED BY KINESIN HEAVY-CHAIN OR KIF3A/B. *Journal of Cell Biology*. 129:157-167.

Patel, J.T., H.R. Belsham, A.J. Rathbone, B. Wickstead, C. Gell, and C.T. Friel. 2016. The family-specific alpha 4-helix of the kinesin-13, MCAK, is critical to microtubule end recognition. *Open Biology*. 6.

Piao, T., M. Luo, L. Wang, Y. Guo, D. Li, P. Li, W.J. Snell, and J. Pan. 2009. A microtubule depolymerizing kinesin functions during both flagellar disassembly and flagellar assembly in Chlamydomonas. *Proceedings of the National Academy of Sciences of the United States of America*. 106:4713-4718.

Puri, D., K. Ponniah, K. Biswas, A. Basu, S. Dey, E.A. Lundquist, and A. Ghosh-Roy. 2021. Wnt signaling establishes the microtubule polarity in neurons through regulation of Kinesin-13. *Journal of Cell Biology*. 220.

Song, Y., Y. Zhang, Y. Pan, J. He, Y. Wang, W. Chen, J. Guo, H. Deng, Y. Xue, X. Fang, and X. Liang. 2020. The microtubule end-binding affinity of EB1 is enhanced by a dimeric organization that is susceptible to phosphorylation. *Journal of Cell Science*. 133.

Tan, D., W.J. Rice, and H. Sosa. 2008. Structure of the Kinesin13-Microtubule Ring Complex. *Structure*. 16:1732-1739.

Tinevez, J.-Y., N. Perry, J. Schindelin, G.M. Hoopes, G.D. Reynolds, E. Laplantine, S.Y. Bednarek, S.L. Shorte, and K.W. Eliceiri. 2017. TrackMate: An open and extensible platform for single-particle tracking. Methods. 115:80-90.

Tournebize, R., A. Popov, K. Kinoshita, A.J. Ashford, S. Rybina, A. Pozniakovsky, T.U. Mayer, C.E. Walczak, E. Karsenti, and A.A. Hyman. 2000. Control of microtubule dynamics by the antagonistic activities of XMAP215 and XKCM1 in Xenopus egg extracts. *Nature Cell Biology*. 2:13-19.

Trofimova, D., M. Paydar, A. Zara, L. Talje, B.H. Kwok, and J.S. Allingham. 2018. Ternary complex of Kif2A-bound tandem tubulin heterodimers represents a kinesin-13-mediated microtubule depolymerization reaction intermediate. *Nature Communications*. 9.

Vasudevan, K.K., Y.-Y. Jiang, K.F. Lechtreck, Y. Kushida, L.M. Alford, W.S. Sale, T. Hennessey, and J. Gaertig. 2015. Kinesin-13 regulates the quantity and quality of tubulin inside cilia. *Molecular Biology of the Cell*. 26:478-494.

Vitre, B., F.M. Coquelle, C. Heichette, C. Garnier, D. Chretien, and I. Arnal. 2008. EB1 regulates microtubule dynamics and tubulin sheet closure in vitro. *Nature Cell Biology*. 10:415-U481.

Walczak, C.E., E.C. Gan, A. Desai, T.J. Mitchison, and S.L. Kline-Smith. 2002. The microtubule-destabilizing kinesin XKCM1 is required for chromosome positioning during spindle assembly. *Curr. Biol.* 12:1885-1889.

Walczak, C.E., T.J. Mitchison, and A. Desai. 1996. XKCM1: a Xenopus kinesin-related protein that regulates microtubule dynamics during mitotic spindle assembly. *Cell*. 84:37-47.

Wang, W., S. Cantos-Fernandes, Y. Lv, H. Kuerban, S. Ahmad, C. Wang, and B. Gigant. 2017. Insight into microtubule disassembly by kinesin-13s from the structure of Kif2C bound to tubulin. *Nature Communications*. 8.

Wang, W., T. Shen, R. Guerois, F. Zhang, H. Kuerban, Y. Lv, B. Gigant, M. Knossow, and C. Wang. 2015. New Insights into the Coupling between Microtubule Depolymerization and ATP Hydrolysis by Kinesin-13 Protein Kif2C. *Journal of Biological Chemistry*. 290:18721-18731.

Widlund, P.O., M. Podolski, S. Reber, J. Alper, M. Storch, A.A. Hyman, J. Howard, and D.N. Drechsel. 2012. One-step purification of assembly-competent tubulin from diverse eukaryotic sources.

Molecular Biology of the Cell. 23:4393-4401.

Wittmann, T., A. Hyman, and A. Desai. 2001. The spindle: a dynamic assembly of microtubules and motors. *Nature Cell Biology*. 3:E28-E34.

Wordeman, L., and T.J. Mitchison. 1995. IDENTIFICATION AND PARTIAL CHARACTERIZATION OF MITOTIC CENTROMERE-ASSOCIATED KINESIN, A KINESIN-RELATED PROTEIN THAT ASSOCIATES WITH CENTROMERES DURING MITOSIS. *Journal of Cell Biology*. 128:95-105.

Zong, H., M. Hazelbaker, C. Moe, S.C. Ems-McClung, K. Hu, and C.E. Walczak. 2021. Spatial regulation of MCAK promotes cell polarization and focal adhesion turnover to drive robust cell migration. *Molecular Biology of the Cell*. 32:590-604.

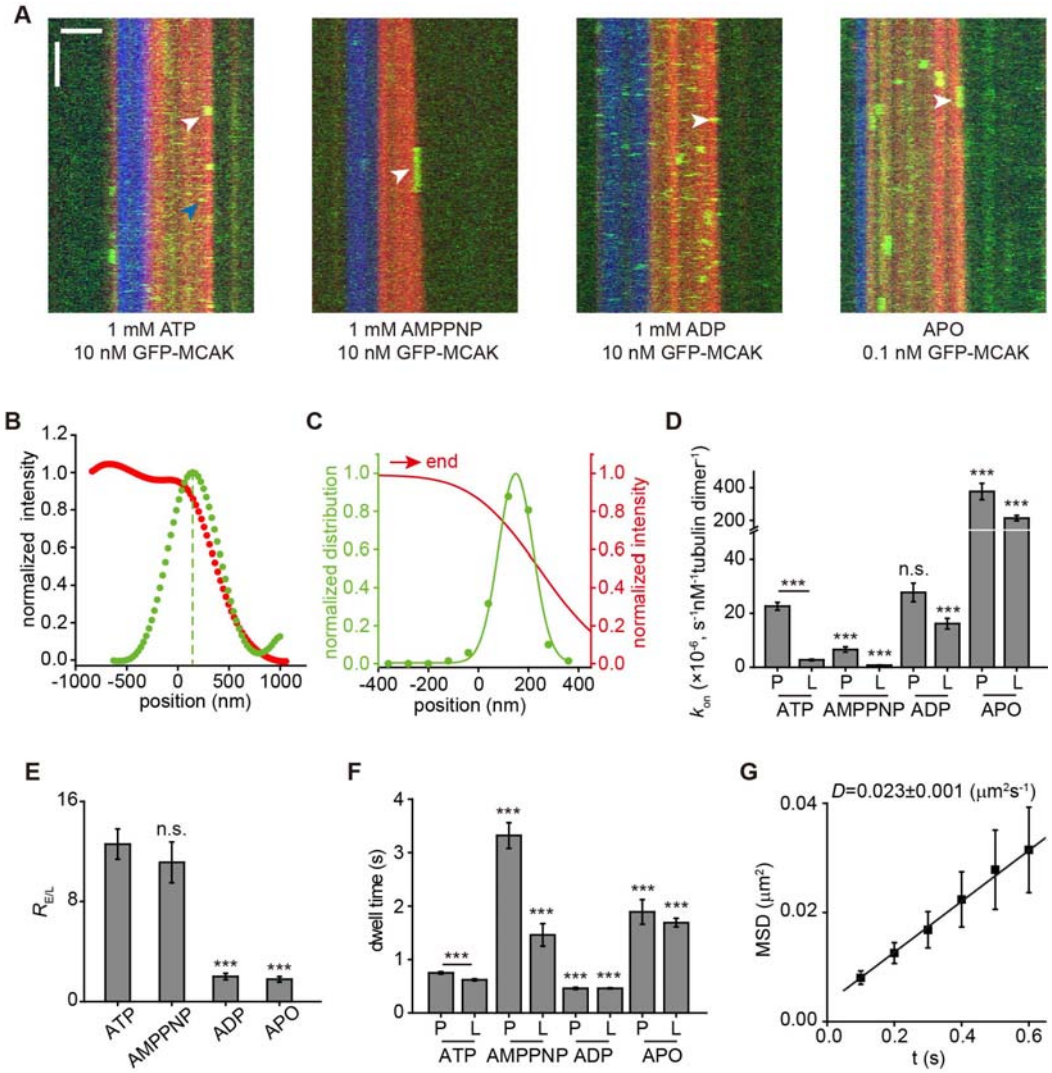

Figure 1. MCAK preferentially binds to growing microtubule ends

(A) The representative kymographs of single-molecule GFP-MCAK (green) binding events on dynamic microtubules (red, tubulin: 16 μM) growing from GMPCPP microtubule seeds (blue) in the presence of 1 mM ATP, AMPPNP, ADP and APO (the nucleotide-free state). The binding events at the plus-end and lattice were indicated by a white arrowhead and a blue arrowhead, respectively. Vertical bar: 5 s; horizontal bar: 2 μm.

(B) The plot showing the representative intensity profiles of a single GFP-MCAK molecule (green) and a growing microtubule end (red). The peak position of a GFP-MCAK molecule was recorded as the binding location (dashed line in green).

(C) The spatial distributions of the binding sites of GFP-MCAK (green, n=152 events) along the long axis of microtubules. The averaged intensity profile of the growing

731 microtubule ends (red) was shown as the positional reference.

732 **(D)** Statistical quantification of the apparent association constant (k_{on}) of GFP-MCAK
733 on the plus-end and lattice of dynamic microtubules in the presence of 1 mM ATP
734 (n=66 microtubules from 3 assays), AMPPNP (n=29 microtubules from 2 assays),
735 ADP (n=21 microtubules from 2 assays) and APO (n=36 microtubules from 3 assays).
736 The statistical comparison was made versus the k_{on} of MCAK on the corresponding
737 location (i.e. plus end or lattice) in the ATP condition.

738 **(E)** Statistical quantification of $R_{E/L}$ in the presence of ATP, AMPPNP, ADP and APO.
739 The statistical comparison was made versus the $R_{E/L}$ of the plus-end binding events in
740 the ATP condition.

741 **(F)** Statistical quantification of the dwell time of GFP-MCAK on the growing end
742 and lattice of dynamic microtubules in the presence of ATP (n=966 events from 3 as-
743 says for the plus end; n=702 events from 3 assays for lattice), AMPPNP (n=231
744 events from 2 assays for the plus end; n=142 events from 2 assays for lattice), ADP
745 (n=327 events from 2 assays for the plus end; n=1184 events from 2 assays for lattice)
746 and APO (n=71 events from 3 assays for the plus end; n=573 events from 3 assays for
747 lattice). The statistical comparison was made versus dwell time of the binding events
748 on the corresponding location (i.e. plus end or lattice) in the ATP condition.

749 **(G)** The mean-squared displacement (MSD) of GFP-MCAK was plotted against the
750 time interval (t, 0.1s per frame). The diffusion coefficient (D) of 0. 023 $\mu m^2 s^{-1}$ was
751 obtained using a linear fitting ($<x^2>= 2Dt$). The error bar represented SEM (n=203
752 trajectories).

753 In panel **D**, **E** and **F**, all the data were presented as mean ± SEM. All the comparisons
754 were performed using the two-tailed Mann-Whitney U test with Bonferroni correction,
755 n.s., no significance; ***, $p<0.001$.

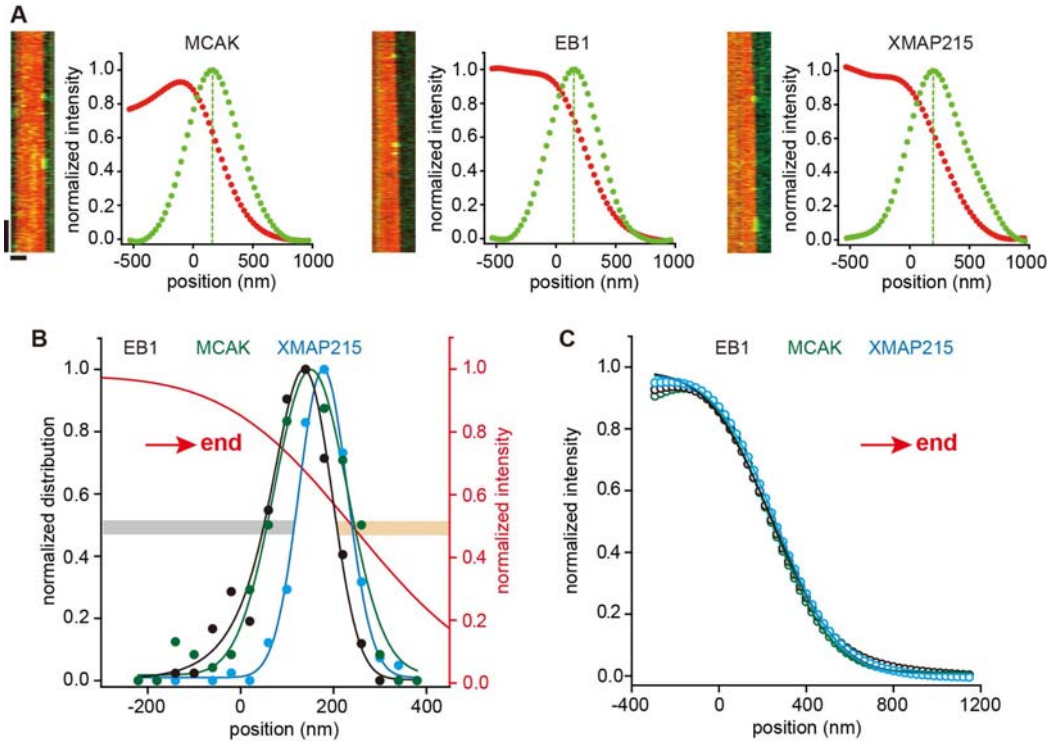

Figure 2. MCAK binds to the entire GTP cap of growing microtubule ends

(**A**) The representative kymograph showing the individual binding events of GFP-MCAK (1 nM, with 1 mM ATP, left), EB1-GFP (10 nM, middle) or XMAP215-GFP (1 nM, right) at growing microtubule ends (red, tubulin: 12 μM). The plots showed the representative intensity profiles of a single molecule (green) and a growing microtubule end (red). The peak position of individual molecules was determined using a Gaussian fit (dashed line in green). Vertical bar: 5 s; horizontal bar: 2 μm.

(**B**) The spatial distributions of the binding sites of GFP-MCAK (green, n=123 events), EB1-GFP (black, n=184 events) and XMAP215-GFP (blue, 142 events) along the long axis of microtubules. The averaged intensity profile of the growing microtubule ends (red) was shown as the positional reference. The region within the FWHM of the blue curve was considered to be the binding region of XMAP215. The MCAK molecules localized to the left of this region was considered to be proximally distributed (grey bar). The region within the FWHM of the black curve was considered to be the binding region of EB1. The MCAK molecules localized to the right of this region was considered to be distally distributed (orange bar).

(**C**) The averaged intensity profiles of the growing microtubule ends were used to quantify the localization of GFP-MCAK (green, 123 microtubules), EB1-GFP (black, 184 microtubules) and XMAP215-GFP (blue, 142 microtubules). Note that the morphologies of microtubule ends in three conditions were nearly identical. In panels **B** and **C**, the red arrows indicated the direction of microtubule growth.

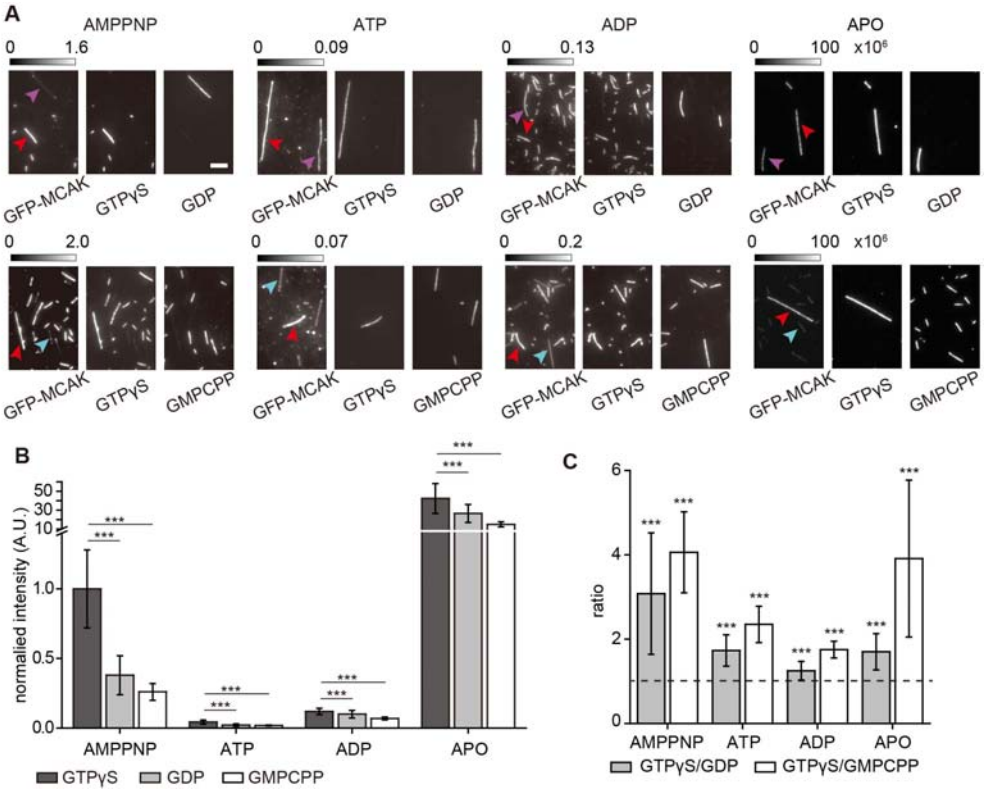

Figure 3. MCAK strongly binds to GTPγS microtubules in a nucleotide-independent manner

(A) The representative projection images of GFP-MCAK binding to GTPγS (red arrowhead), GDP (purple arrowhead) and GMPCPP microtubules (cyan arrowhead) in the presence of 1 mM AMPPNP (left), 1 mM ATP (left middle), 1 mM ADP (right middle) and at the APO state (right). Note that the binding on GDP or GMPCPP microtubules was compared to that on GTPγS microtubules in the same flow cell. Scale bar: 5 μm.

(B) Statistical comparison of the normalized fluorescence intensity of GFP-MCAK on different microtubules in the presence of 1 mM AMPPNP (112 GTPγS microtubules, 56 GMPCPP microtubules, 56 GDP microtubules from 3 assays), 1 mM ATP (88 GTPγS microtubules, 60 GMPCPP microtubules, 28 GDP microtubules from 3 assays), 1 mM ADP (95 GTPγS microtubules, 51 GMPCPP microtubules, 44 GDP microtubules from 3 assays) or at the APO state (66 GTPγS microtubules, 30 GMPCPP microtubules, 36 GDP microtubules from 3 assays). All data were normalized to the binding intensity of GFP-MCAK (1 nM) on GTPγS microtubules in the AMPPNP condition.

(C) The ratios of the binding intensity of GFP-MCAK on GTPγS microtubules to that on GDP or GMPCPP microtubules in various nucleotide conditions. The dashed line

on the plot represented 1. The statistical comparisons were performed between the ratios and 1.

In panel **B** and **C**, All the data were presented as mean ± std. All the comparisons were performed using the two-tailed Mann–Whitney U test with Bonferroni correction, ***, $p<0.001$.

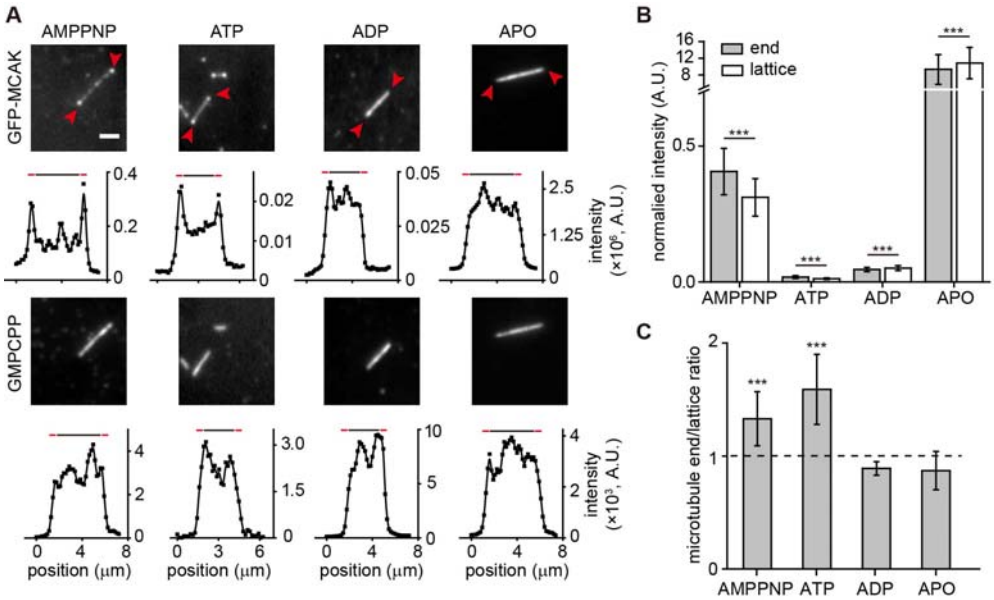

Figure 4. MCAK strongly binds to the ends of GMPCPP microtubules in a nucleotide state-dependent manner

(A) The representative projection images and intensity profiles showing GFP-MCAK binding (upper) at the ends of GMPCPP microtubules (lower) in the presence of 1 mM AMPPNP (left), 1 mM ATP (left middle), 1 mM ADP (right middle) or at the APO state (right). Red arrowhead: the end-binding of MCAK. Red bar: ends. Black bar: lattice. Scale bar=2 μm.

(B) Statistical quantification of the binding intensity of GFP-MCAK on the lattice and end of GMPCPP microtubules in the presence of 1 mM AMPPNP (47 microtubules from 3 assays), 1 mM ATP (40 microtubules from 3 assays), 1 mM ADP (45 microtubules from 3 assays) or at the APO state (52 microtubules from 3 assays). All data were normalized to the binding of GFP-MCAK (1 nM) on GTPγS microtubules in the AMPPNP condition. All the data were presented as mean ± std. The statistical analysis was performed using the two-tailed pair *t*-test by Bonferroni correction, ***, $p<0.001$.

(C) The ratios between the binding intensity of GFP-MCAK at the end and the intensity on the lattice of GMPCPP microtubules in various nucleotide conditions. The ratios were presented as mean ± std. The dashed line on the plot represents 1. The statistical comparisons were performed between the ratios and 1 using the two-tailed Mann-Whitney U test with Bonferroni correction, ***, $p<0.001$.

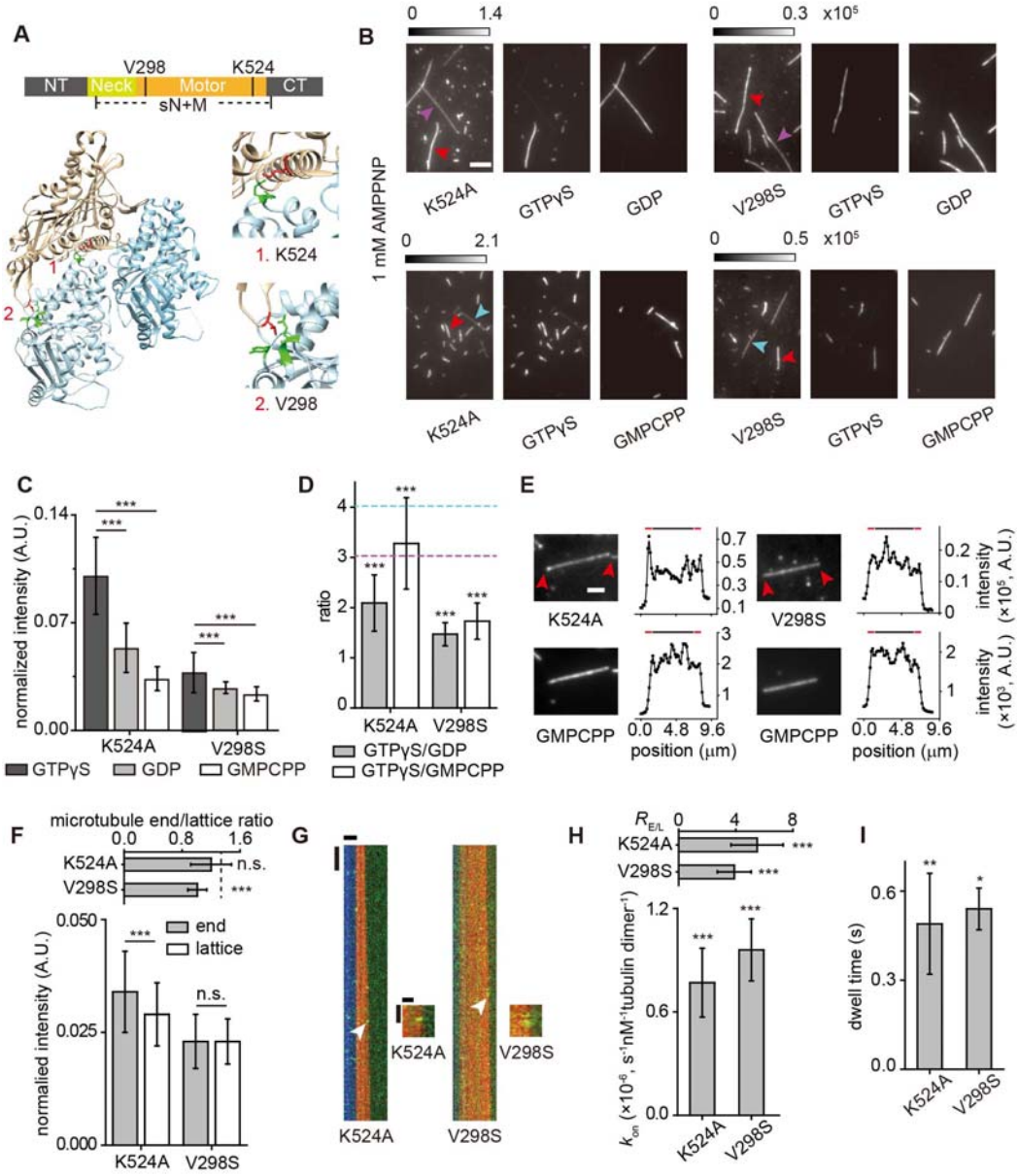

Figure 5. The preference for GDP·Pi-tubulins facilitates the binding preference of MCAK for growing microtubule ends

(A) The structural model of the MCAK^{sN+M}-tubulin complex (PDB ID: 5MIO). The cartoon schematic in upper panel showed the domain organization of MCAK. Loop2 and α4 helix, two regions mediating the interaction between MCAK and tubulin, were enlarged and the key sites (K524, V298) were highlighted in red. The corresponding residues of tubulin that may interact with K524 and V298 were highlighted in green.

(B) The representative projection images of GFP-MCAK^{K524A} and GFP-MCAK^{V298S} binding to GTPγS (red arrowhead), GDP (purple arrowhead) and GMPCPP microtubules (cyan arrowhead) in the presence of 1 mM AMPPNP. Scale bar: 5 μm.

837 **(C)** Statistical quantification of the binding intensity of GFP-MCAK^{K524A} (144
838 GTPγS microtubules, 72 GMPCPP microtubules, 62 GDP microtubules from 3 assays)
839 and GFP-MCAK^{V298S} (124 GTPγS microtubules, 65 GMPCPP microtubules, 59 GDP
840 microtubules from 3 assays) on different microtubules. Note that all data were nor-
841 malized to the binding intensity of GFP-MCAK on GTPγS microtubules in the
842 AMPPNP condition. The data were presented as mean ± std.

843 **(D)** The ratios of the binding intensity of GFP-MCAK^{K524A} or GFP-MCAK^{V298S} on
844 GTPγS microtubules to that on GDP or GMPCPP microtubules in the presence of 1
845 mM AMPPNP. Purple dashed line: The GTPγS/GDP ratio of GFP-MCAK. The cyan
846 dashed line: the GTPγS/GMPCPP ratio of GFP-MCAK. The data were presented as
847 mean ± std. The statistical comparisons were made versus the corresponding value of
848 GFP-MCAK.

849 **(E)** The representative projection images and intensity profiles showing the binding
850 of GFP-MCAK^{K524A} and GFP-MCAK^{V298S} to the end (red arrowhead in the upper
851 panels) and lattice of GMPCPP microtubules (lower panels) in the presence of
852 AMPPNP. Red bar: ends. Black bar: lattice. Scale bar=2 μm.

853 **(F)** Statistical quantification of the binding intensity of GFP-MCAK^{K524A} (88 micro-
854 tubules from 3 assays) and GFP-MCAK^{V298S} (68 microtubules from 3 assays) on the
855 lattice and end of GMPCPP microtubules in the presence of AMPPNP (lower panel).
856 All the data were normalized to the binding of GFP-MCAK (1 nM) on GTPγS micro-
857 tubules in the AMPPNP condition. All the binding intensity data were presented as
858 mean ± std. The statistical analyses were performed using the two-tailed paired *t*-test
859 by Bonferroni correction, n.s., no significance; ***, $p<0.001$. The inset (upper) show-
860 ing the ratios of the end-binding intensity of GFP-MCAK^{K524A} or GFP-MCAK^{V298S} to
861 the lattice-binding intensity on GMPCPP microtubules in the presence of AMPPNP.
862 The ratios were presented as mean ± std. The statistical comparisons were made ver-
863 sus the ratio of GFP-MCAK (the dashed line shown in **Fig. 4C**).

864 **(G)** The representative kymographs of the single-molecule binding events of
865 GFP-MCAK^{K524A} (10 nM, green) and GFP-MCAK^{V298S} (30 nM, green) on growing
866 microtubules (red, tubulin: 16 μM) in the presence of 1 mM ATP. The end-binding
867 events were indicated using white arrowheads and enlarged. For the original kymo-
868 graphs, vertical bar: 2 s; horizontal bar: 2 μm. For the enlarged kymographs, vertical
869 bar: 1 s; horizontal bar: 0.5 μm.

870 **(H)** Statistical quantification of the apparent association constant ($k_{on\text{-}P}$) of
871 GFP-MCAK^{K524A} (33 microtubules from 3 assays) and GFP-MCAK^{V298S} (23 micro-
872 tubules from 2 assays) on growing microtubule ends in the presence of ATP (lower).
873 The statistical comparisons were made versus the $k_{on\text{-}P}$ of GFP-MCAK. The inset
874 (upper) showing the statistical quantification of $R_{E/L}$ of GFP-MCAK^{K524A} and
875 GFP-MCAK^{V298S}. The $R_{E/L}$ of both mutants were compared to that of GFP-MCAK in
876 the ATP condition. All the data were presented as mean ± SEM.

877 **(I)** Statistical quantification of the dwell time of GFP-MCAK^{K524A} (19 binding events
878 from 3 assays) and GFP-MCAK^{V298S} (43 binding events from 3 assays) on growing
879 microtubule ends in the presence of ATP. The dwell time were presented as mean ±
880 SEM. The dwell time of GFP-MCAK^{K524A} and GFP-MCAK^{V298S} were compared to
881 that of GFP-MCAK.

882 In panel **C**, **D**, **F** (the upper inset), **H** and **I**, all the comparisons were performed using
883 the two-tailed Mann-Whitney U test with Bonferroni correction, n.s., no significance;
884 *, $p<0.05$; **, $p<0.01$; ***, $p<0.001$.

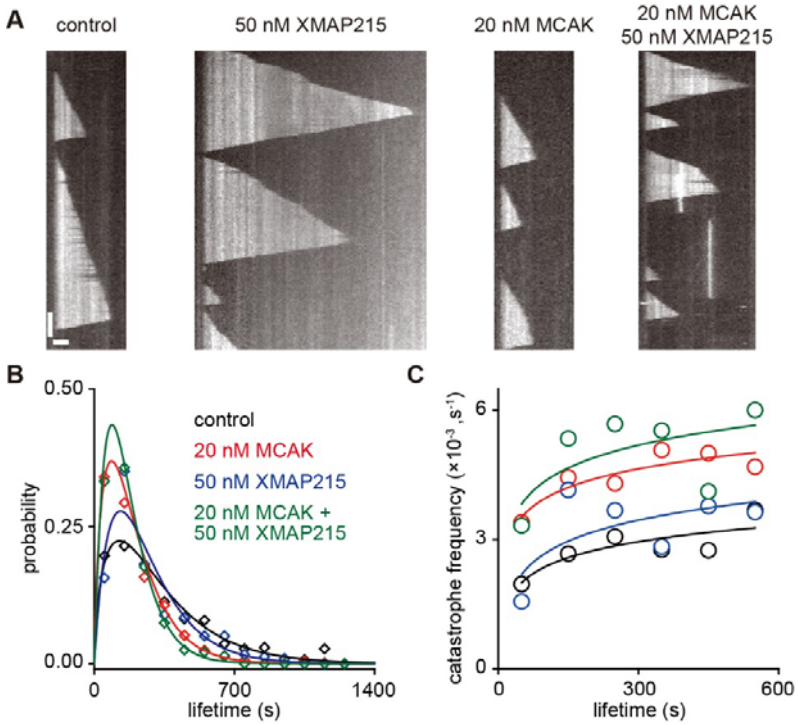

Figure 6. Functional specification of MCAK and XMAP215 at growing microtubule ends

(**A**) The representative kymographs of dynamic microtubules (tubulin: 10 µM) in the control condition or in the presence of MCAK, XMAP215 or both. Vertical bar: 100 s; horizontal bar: 2 µm.

(**B**) The probability distribution of microtubule lifetime in the experimental conditions indicated in the panel **A**. The lines were gamma fitting curves. Control: 443 microtubules from 7 assays. 20 nM MCAK: 621 microtubules from 7 assays. 50 nM XMAP215: 237 microtubules from 3 assays. 20 nM MCAK+50 nM XMAP215: 283 microtubules from 3 assays.

(**C**) The plots of catastrophe frequency versus the lifetime of microtubules showing how the likelihood of catastrophe depended on the age of microtubules. The data were from the experiments shown in panel **A**.

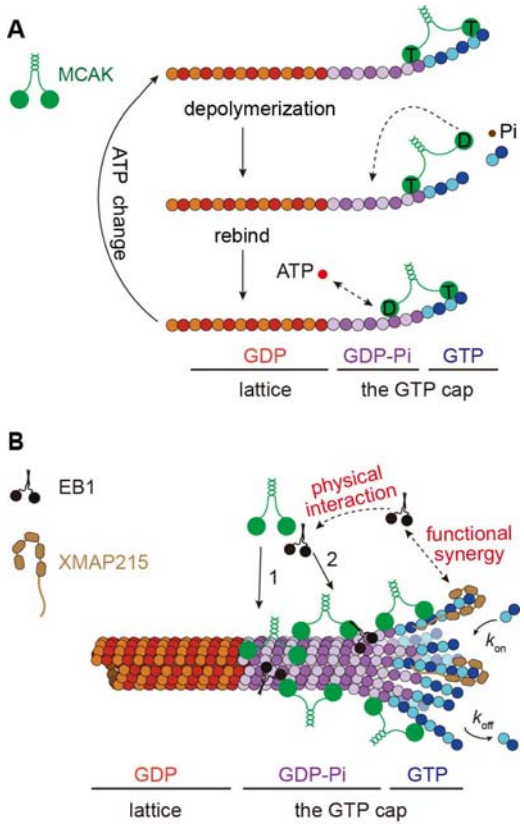

Figure 7. Cartoon schematics depicting the working model of MCAK at growing microtubule ends

(A) A hypothetic model for the binding cycle of MCAK, given its binding preference on the EB cap. T: MCAK·ATP. D: MCAK·ADP.

(B) The co-operation schematics of MCAK, EB1 and XMAP215 at growing microtubule ends. Pathway 1: the direct binding of MCAK to microtubule ends. Pathway 2: the indirect binding of MCAK to microtubule ends via EB1.

Supplementary Information Appendix

Title:

Recognition of the Nucleotide-Dependent Feature Facilitates the Microtubule End-Binding of MCAK

Authors and affiliations:

Wei Chen[1] (chenwill@mail.tsinghua.edu.cn)
Yin-Long Song[1] (y.song4@uu.nl)
Jian-Feng He[1] (jianfenghe2015@mail.tsinghua.edu.cn)
Xin Liang[1,*] (xinliang@tsinghua.edu.cn)

[1] IDG/McGovern Institute for Brain Research, School of Life Sciences, Tsinghua University, Beijing 100084, China

Corresponding author:

Name: Xin Liang
Address: Room E118, Medical School, Tsinghua University, 100084 Beijing, China
Tel: +86-10-62772563
Email: xinliang@tsinghua.edu.cn
ORCID: 0000-0001-7915-8094

Supplementary materials:

Figures s1-s4 (with legends)

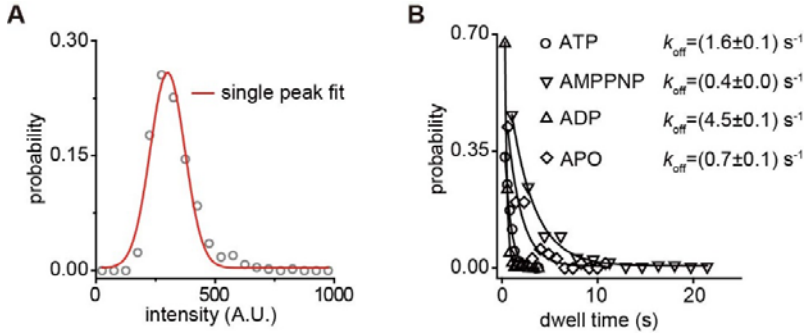

Figure s1. Single-molecule fluorescence analysis and the apparent off-rates (k_{off}) of GFP-MCAK

(A) The fluorescence intensity distribution of GFP-MCAK (red, n=509 binding events) was fitted using a Gaussian function. The background intensity was subtracted. The intensity range ($\mu \pm 2\sigma$=300 ± 145 A.U.) was used to determine if a fluorescence spot represents a single dimer.

(B) The apparent off-rate (k_{off}) of GFP-MCAK on growing microtubule ends in the presence of ATP (minus end, square; plus end, circle), AMPPNP (down triangle), ADP (up triangle) and APO (diamond). k_{off} was calculated by fitting the dwell time of individual GFP-MCAK binding events to a single exponential function.

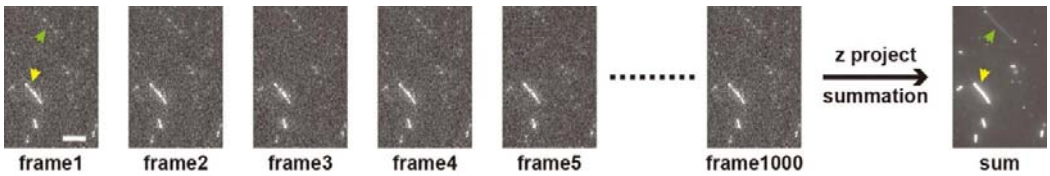

Figure s2. Projection of single-molecule fluorescence images

The representative images showing how to generate a summation image using 1000 frames of raw images. The GDP and GTPγS microtubule were indicated using green and yellow arrowheads, respectively. The concentration of GFP-MCAK here was 1 nM. The experiment was performed in the presence of 1 mM AMPPNP. Scale bar: 5 μm.

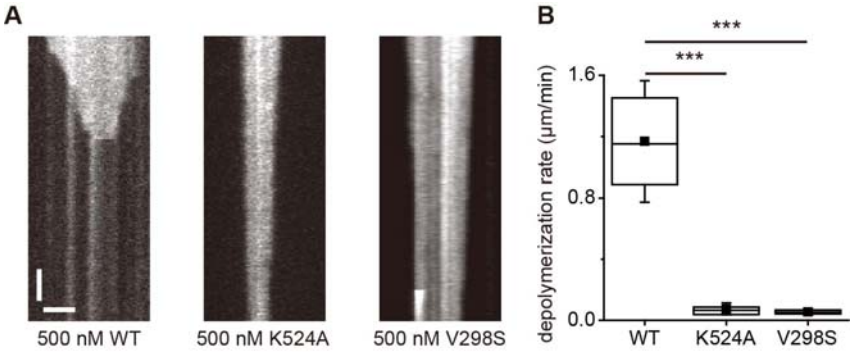

Figure s3. GFP-MCAK^{K525A} and GFP-MCAK^{V298S} are depolymerizing-deficient mutants

(A) The representative kymographs showing the depolymerizing effect of GFP-MCAK, GFP-MCAK^{K525A} and GFP-MCAK^{V298S} on GMPCPP-stabilized microtubules in the presence of 1 mM ATP. Vertical bar: 100 s, horizontal bar: 2 µm.

(B) Statistical quantification of the depolymerization rates of GFP-MCAK (*n*=21 microtubules from 3 assays), GFP-MCAK^{K525A} (*n*=11 microtubules from 2 assays) and GFP-MCAK^{V298S} (*n*=52 microtubules from 3 assays). The data were presented as mean ± std. The statistical analysis was performed using the two-tailed Mann-Whitney U test with Bonferroni correction, ***, $p<0.001$.

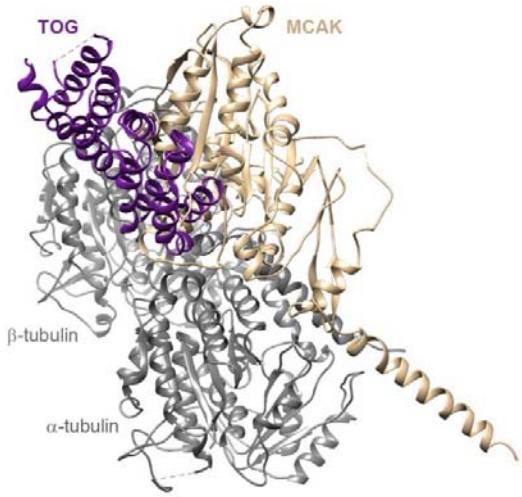

Figure s4. Structural models showing the kinesin-13-tubulin contact site and the TOG-tubulin contact site

The structural model showing that the TOG domain (PDB ID: 4FFB) and the motor domain of MCAK (PDB ID: 6BBN) shared, to some extent, the binding site on a tubulin dimer.